

Supporting Information

Understanding interplay of defects, oxygen, and strain in 2D materials for next-generation optoelectronics

Keerthana S Kumar¹, Ajit Kumar Dash¹, Hasna Sabreen H², Manvi Verma¹, Vivek Kumar¹, Kenji Watanabe³, Takashi Taniguchi⁴, Gopalakrishnan Sai Gautam², Akshay Singh^{1,*}

¹Department of Physics, Indian Institute of Science, Bengaluru, Karnataka -560012, India

²Department of Materials Engineering, Indian Institute of Science, Bengaluru, Karnataka -560012, India

³Research Center for Functional Materials, National Institute for Materials Science, Ibaraki 305-0044, Japan

⁴International Center for Materials Nanoarchitectonics, National Institute for Materials Science, Ibaraki 305-0044, Japan

*Corresponding author: aksy@iisc.ac.in

I) Optical microscope images of exfoliated samples and hBN covered oxygen assisted chemical vapor deposition (O-CVD) sample:

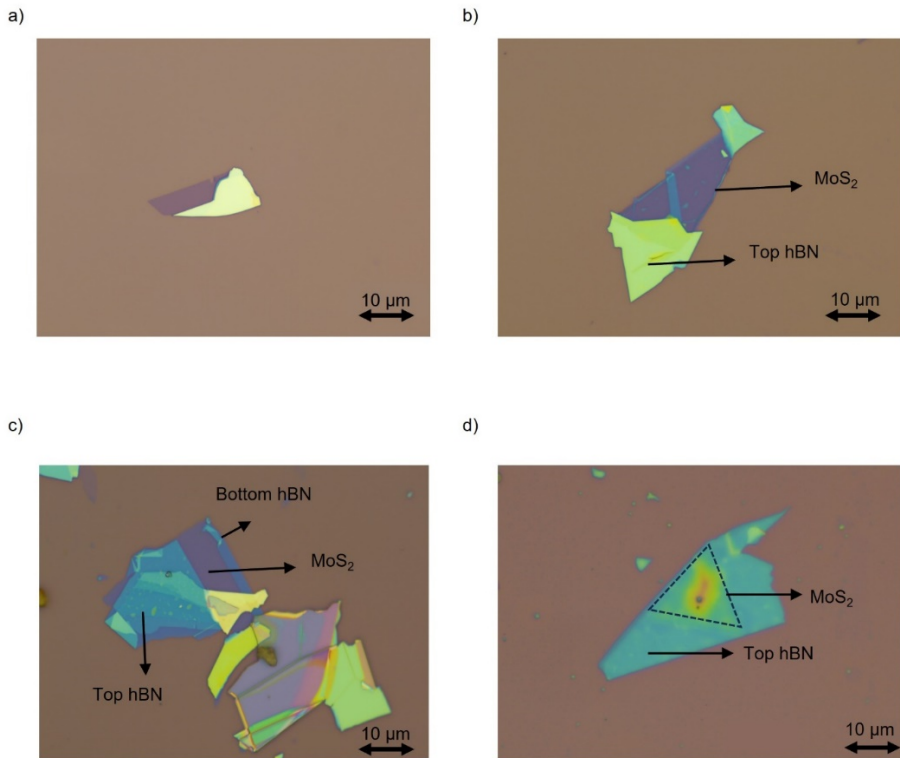


Figure S-I. Optical microscope images of monolayer (ML)-MoS₂ samples a) S1 b) S2 c) S3 d) S5 discussed in Main text. The light purple contrast corresponds to monolayer MoS₂ as labelled in the images, and is clearly distinguishable from the substrate contrast as well as the contrast of bulk MoS₂ and hBN.

II) Schematics of different types of defects in monolayer (ML)-MoS₂:

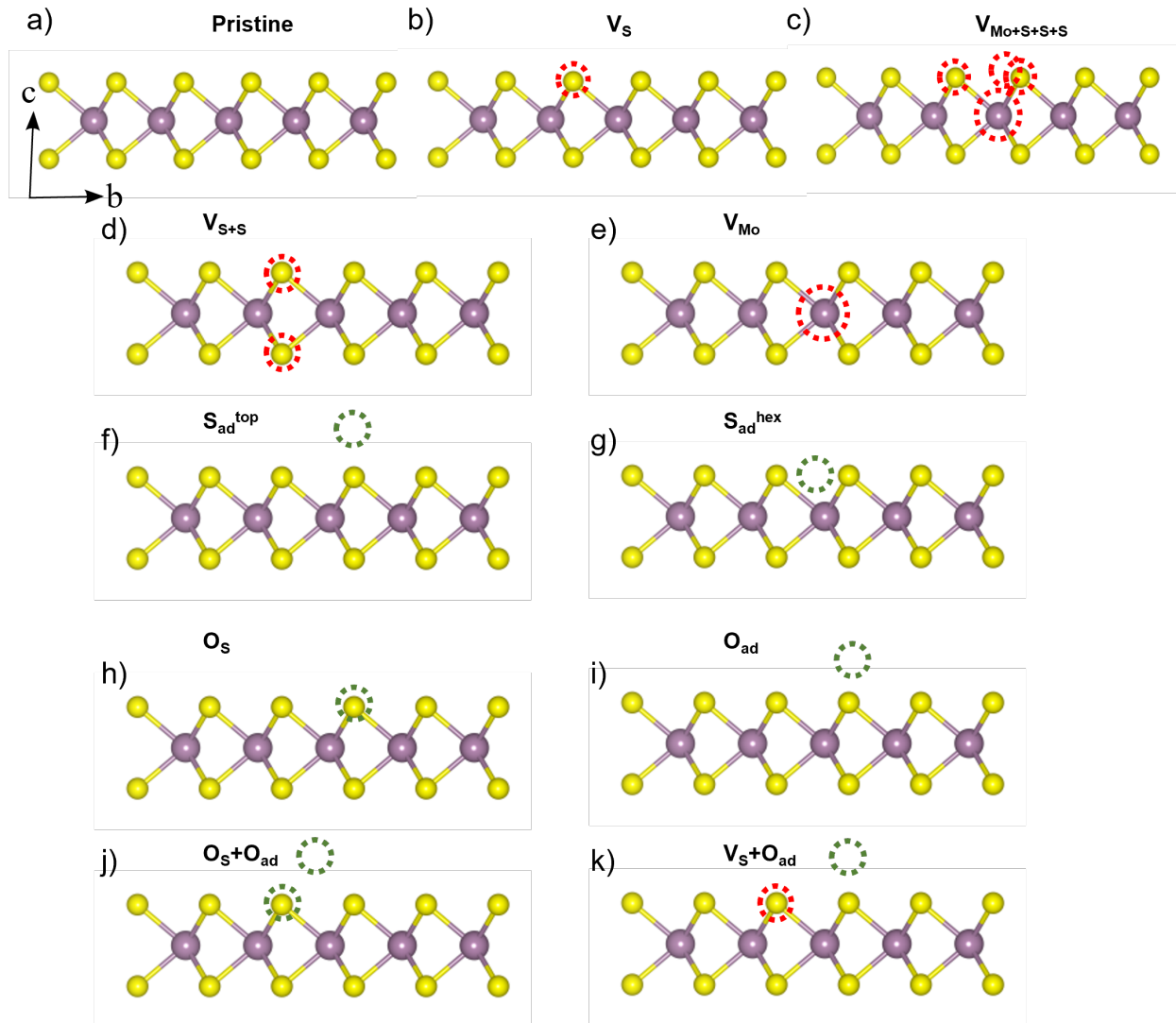


Figure S-II. Initial atomic structures of (a) pristine ML-MoS₂, ML-MoS₂ with (b) mono S vacancy (Vs), (c) Mo-S₃ vacancy cluster (Vmots+s+s). (d) di-S vacancy (along the top and bottom of the ML–Vs+s), (e) mono Mo vacancy (Vm). Red dotted circles indicate that particular atom is missing, (f) S adatom on top of S (S_{ad}^{top}), (g) S adatom in the hexagonal void between S atoms (S_{ad}^{hex}), (h) O antisite at S (Os), (i) O adatom on top of S (O_{ad}) , (j) O antisite at S and O adatom on top of S (Os + O_{ad}) and k) S vacancy and O adatom on top of S (Vs + O_{ad}). The yellow and purple spheres indicate S, Mo respectively. For each structure, cross-sectional ($b - c$ plane) is shown. The adatoms are initialized at a distance of 2 Å from the nearest atom on the ML along the c -axis.

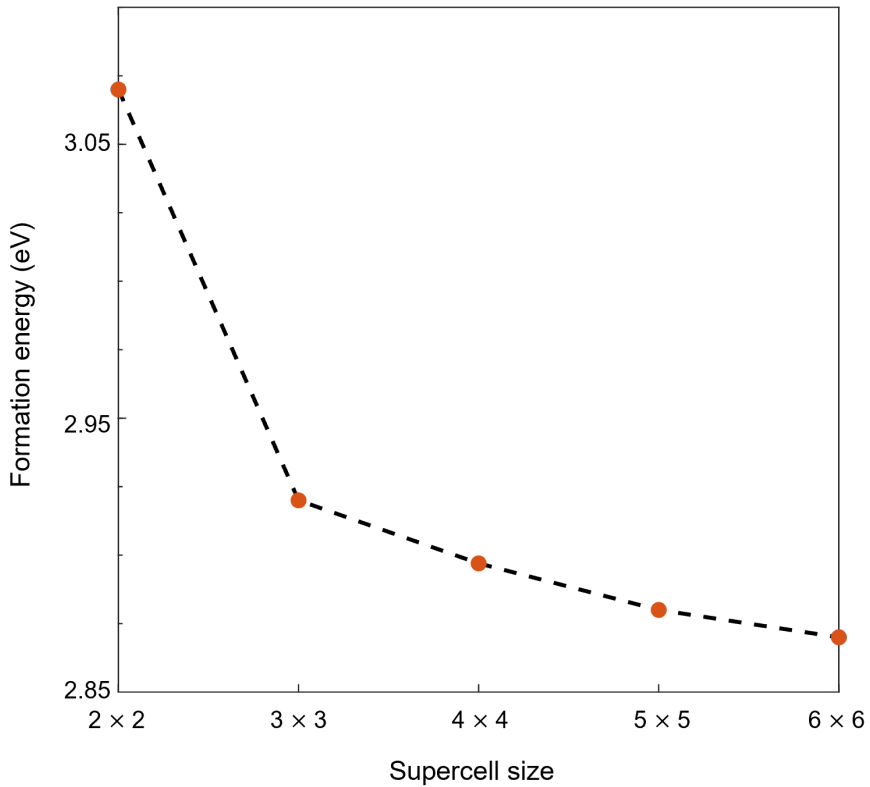


Figure S-III. Change in formation energy with the supercell size for a sulphur vacancy (Vs) defect in monolayer (ML) MoS₂. The formation energy converges to within ~0.1 eV at the 4×4 supercell, with respect to the larger 6×6 cell, which is the typical convergence criteria for defect formation energies using computations.^{1,2} All subsequent calculations are hence carried out in a 4×4 cell.

III) Formation energy of defects in monolayer MoS₂ in different growth conditions:

The defect formation energies were calculated using

$$E_{\text{defect}}^f = E_{\text{defect}} - E_{\text{pristine}} - \sum_i n_i \mu_i + qE_F + E_{\text{corr}}$$

Where E_{defect} and E_{pristine} are the total DFT-SCAN^{3,4} derived energies of defective and a pristine supercell respectively, n_i is the number of atoms of species i being added (> 0) or removed (< 0), μ_i

represents the chemical potential of species i , and E_F and E_{corr} are the Fermi energy of the pristine supercell and electrostatic correction, respectively, which are appropriate for defects of non-zero charge q . As ML-MoS₂ is anisotropic, we use the scheme proposed by Kumagai and Oba⁵, as implemented in the Python charged defect toolkit (PyCDT) to account for the electrostatic corrections⁶.

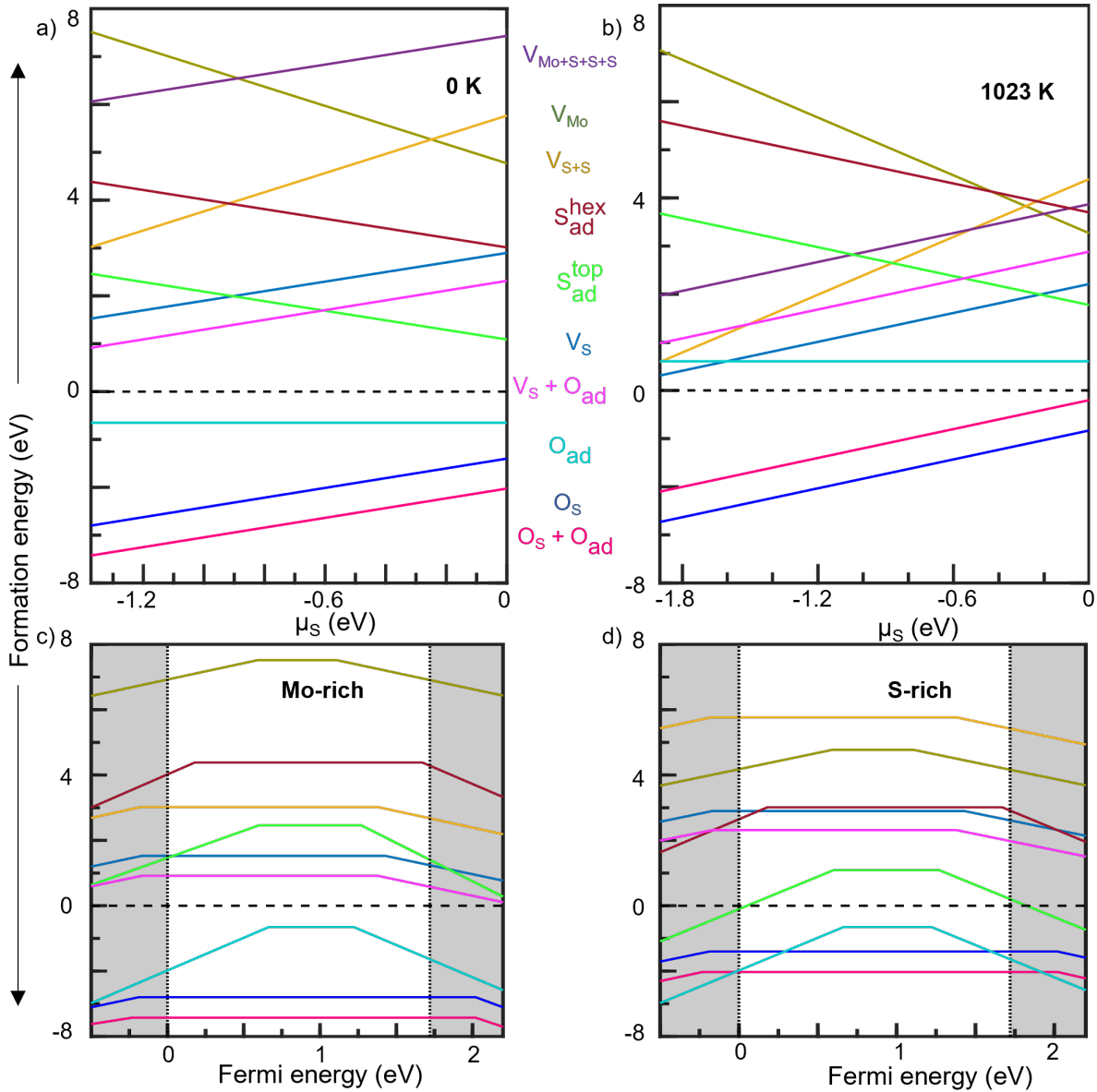


Figure S-IV. Formation energy of different neutral defects at a) 0 K and b) 1023 K, as a function of the sulphur chemical potential (μ_S). Defect transition levels for various charged defects at 0 K under c) Mo-rich ($\mu_S = -1.37$ eV) and d) S-rich conditions ($\mu_S = 0$ eV). The dotted black lines indicate the calculated band edges of pristine ML-MoS₂, which are separated by the bandgap (1.72 eV). The shaded regions indicate the valence and conduction bands of pristine ML-MoS₂.

The formation energy of defects at different temperatures can be estimated by determining the chemical potential (μ_i) of ML-MoS₂, the constituent components Mo and S and the impurity component (O) at a temperature T as

$$\mu_i(T, p) = \mu_i^0(T_0, p_0) + H(T, p_0) - TS(T, p_0) + RT \ln(p_i/p_0)$$

$$\mu_{\text{comp}}^0 = \frac{1}{2} G_{\text{comp}} = \frac{1}{2} H_{\text{comp}} - \frac{1}{2} TS_{\text{comp}}$$

Where $\mu_i^0(T_0, p_0)$ is the reference chemical potential of the compound (component) set to the 0 K DFT energy, p_i is the partial pressure of the component and p_0 is the reference pressure (1 atm). The terms H (T) and S (T) corresponds to the enthalpy and entropy, respectively sourced from the National Institute of Standards and Technology (NIST) database⁷. H (T) is set to 0 at 298 K for pure Mo, S and O, while it is assigned the formation energy of MoS₂ at 298 K.

The change in defect formation energy with chemical potential of S (μ_S) for all the neutral defects at 0 K and at 1023 K (i.e., the temperature maintained during the O-CVD synthesis of ML-MoS₂) is plotted in Figure S-IV (a) and (b) respectively. The range of chemical potential for S (μ_S) varies from -1.37 eV to 0 eV at 0 K to -1.91 eV to 0 eV at 1023 K. Table S-I lists the defect formation energies of various defects in ML-MoS₂ in both Mo- and S-rich conditions at 0 K and 1023 K. From Figure S-IV a, the formation energies of Mo vacancy, MoS₃ vacancy cluster, di-S vacancy, and S adatom (hex) are so high that they will likely not be easily formed in both S- and Mo-rich conditions at 0 K. S vacancy in Mo-rich conditions (1.52 eV) and S adatom in S-rich condition (1.09 eV) at 0 K are the most stable intrinsic point defects with the lowest formation energies as indicated in Figure S-IV a.

The 0 K defect formation energies are negative for all the three O-related defects (O_S , O_{ad} and $O_S + O_{ad}$) suggesting their spontaneous formation. However, at 1023 K, the formation energy of O_{ad} is positive and may not spontaneously form. Comparing the 0 K and 1023 K formation energy plots (Figure S-IV a, b), the vacancy defects show a decrease and the adatom defects show an increase in their formation energies with increase in temperature. The formation energy of V_S decreases to 0.31 eV at Mo-rich conditions at 1023 K whereas the formation of S_{ad}^{top} becomes difficult at higher temperatures due to the increased formation energy (1.78 eV). As we also notice a decrease in the formation of V_{S+S} in Mo-rich conditions at 1023 K, S vacancies are the most abundant intrinsic point defects at these high temperatures. The predominant occurrence of S vacancy due to its lower formation energy is reported in Ref⁸. It is interesting to note that the formation energy of V_{Mo+S+S} significantly reduces from 6.06 eV at 0 K to 1.97 eV at 1023 K in Mo-rich conditions. This decrease in formation energy of V_{Mo+S+S} cluster, compared to V_{Mo} , illustrates that S vacancies can easily form around a Mo vacancy, thus stabilizing the V_{Mo+S+S} cluster at high temperatures.

Defect	Formation energy at 0 K		Formation energy at 1023 K	
	Mo-rich	S-rich	Mo-rich	S-rich
V_S	1.52	2.90	0.31	2.21
V_{Mo}	7.52	4.77	7.07	3.27
V_{S+S}	3.02	5.77	0.59	4.39
V_{Mo+S+S}	6.06	7.43	1.97	3.87
S_{ad}^{top}	2.46	1.09	3.68	1.78
S_{ad}^{hex}	4.38	3.01	5.60	3.70
O_S	-2.80	-1.40	-2.73	-0.83
O_{ad}	-0.65	-0.65	0.60	0.60
O_{ad} ($q = -2$)	-1.63 to 1.82	-1.63 to 1.82	-0.37 to 0.61	-0.37 to 0.61
O_{ad} ($q = +2$)	-1.98 to 1.46	-1.98 to 1.46	-0.73 to 0.61	-0.73 to 0.61

$O_S + O_{ad}$	-3.42	-2.03	-2.10	-0.20
$V_S + O_{ad}$	0.91	2.31	0.98	2.88

Table S-I. Formation energies of various point defects in ML-MoS₂ in Mo- and S-rich conditions at 0 K and 1023 K.

IV) Determination of the electrostatic correction term for charged defect calculations:

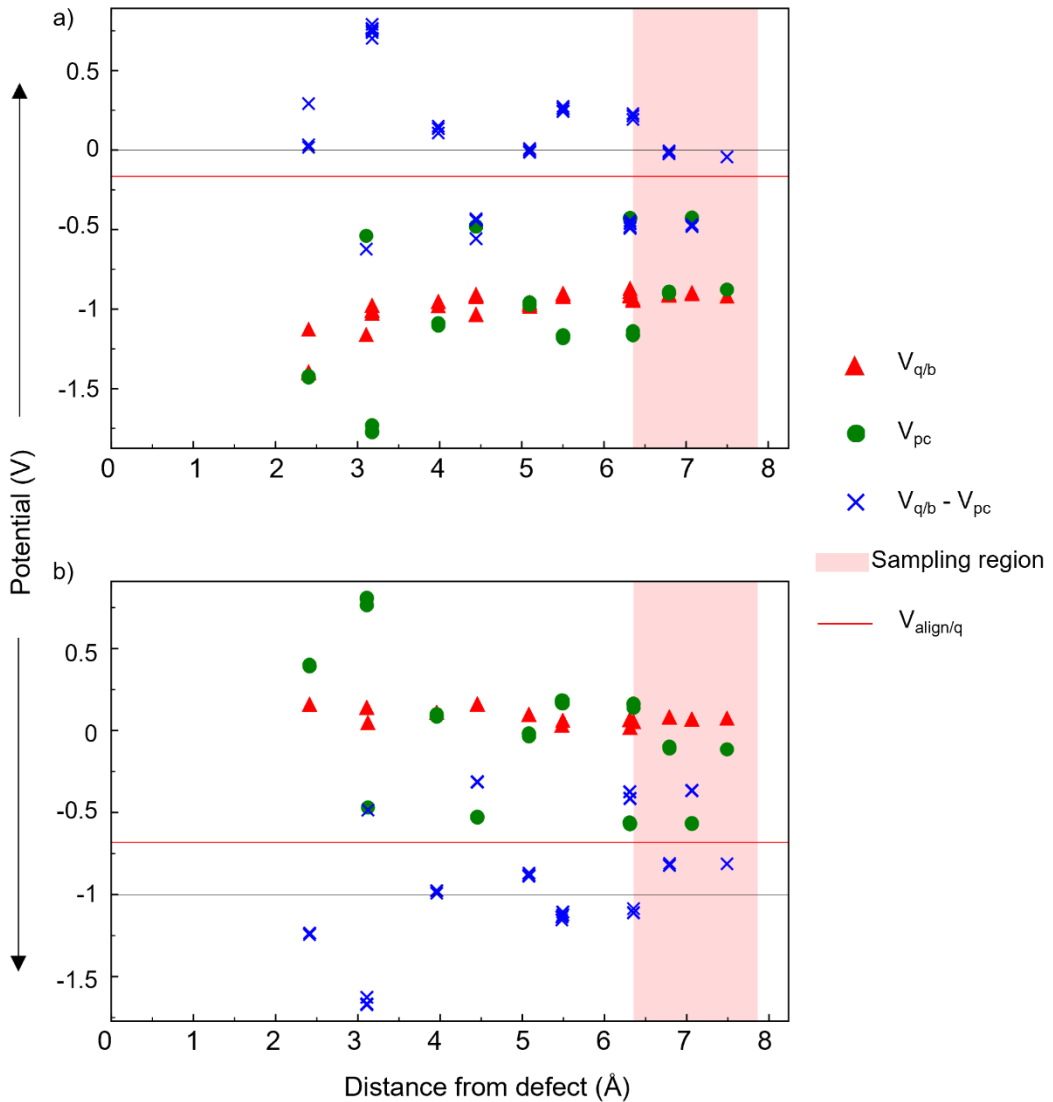


Figure S-V. Schematic of the potential alignment corrections, using the scheme of Kumagai and Oba,⁵ in (a) negatively charged Vs ($q = -1$) and (b) positively charged Vs ($q = +1$). $V_{q/b}$ is the difference in density functional theory (DFT) calculated electrostatic potential between pristine and defective supercells, V_{pc} is the model point-charge potential. $V_{q/b} - V_{pc}$ is the difference between the DFT-calculated potential difference and the point charge potential.

$V_{\text{align/q}}$ reflects the average of $V_{q/b} - V_{pc}$, over the sampling region, which is represented by the shaded region (i.e., the region outside the Wigner-Seitz sphere around the defect). For a negatively charged V_s , the potential alignment term is given by $-q \times V_{\text{align/q}} = 0.16$ eV with a net electrostatic correction (E_{corr}) of -0.12 eV and for a positively charged V_s , the alignment term is +0.32 eV with an E_{corr} of -0.28 eV. We used the python charged defect toolkit (PyCDT)⁶ for post-processing of charged defects calculation and determining E_{corr} .

V) Calculated electronic density of states (DOS) of ML-MoS₂ in the presence of various defects:

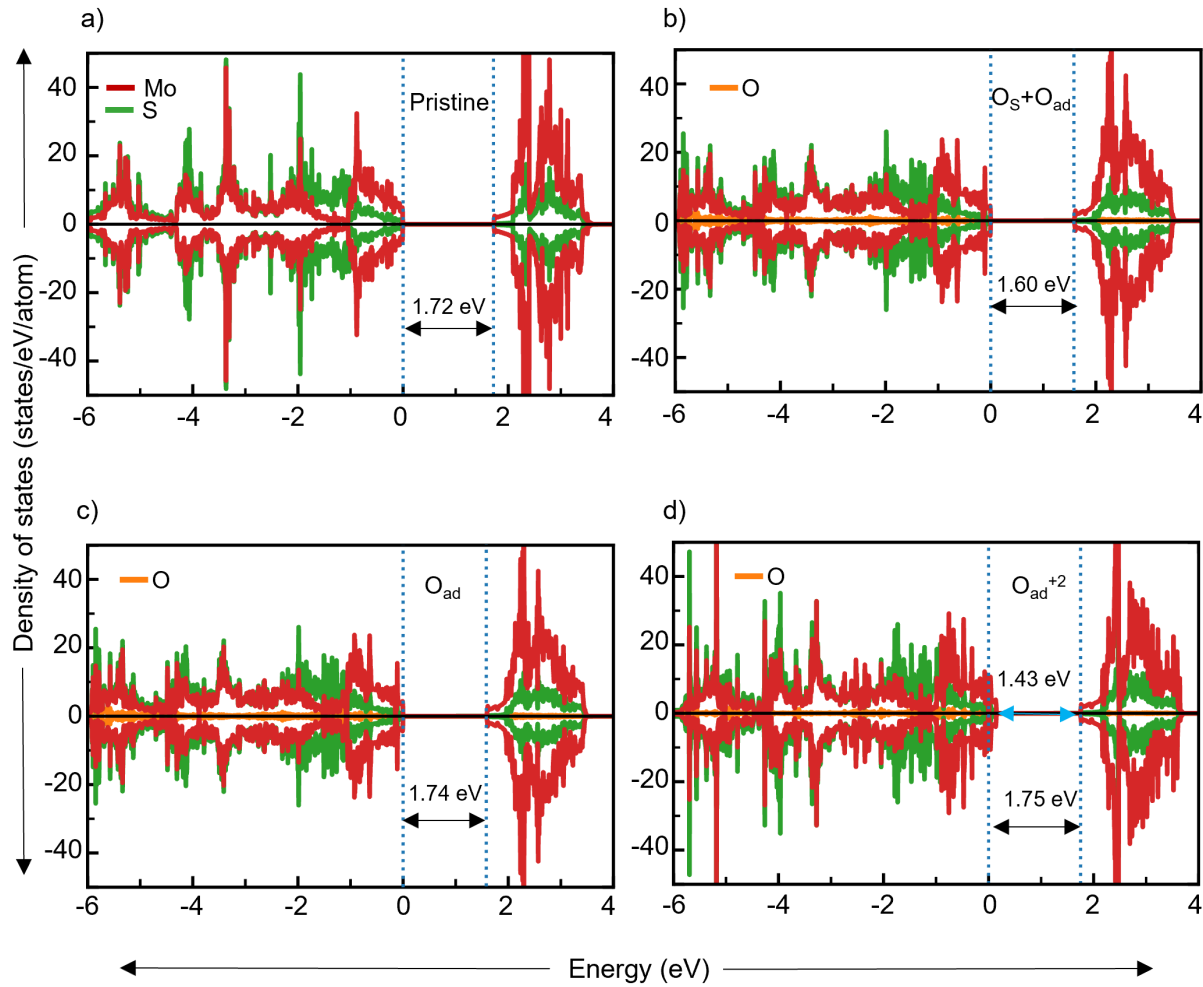


Figure S-VI. Density of states for a) Pristine ML-MoS₂ and MoS₂ with b) O_S + O_{ad}, c) O_{ad}, and d) O_{ad}⁺². The dotted blue lines represent band edges. Mo-d, S-p, and O-p states are represented by red, green, and orange lines, respectively. Bandgap magnitudes are indicated by black arrows and defect levels by blue arrows.

VI) Effect of defects and strain in the band structure and electronic DOS of MoS₂:

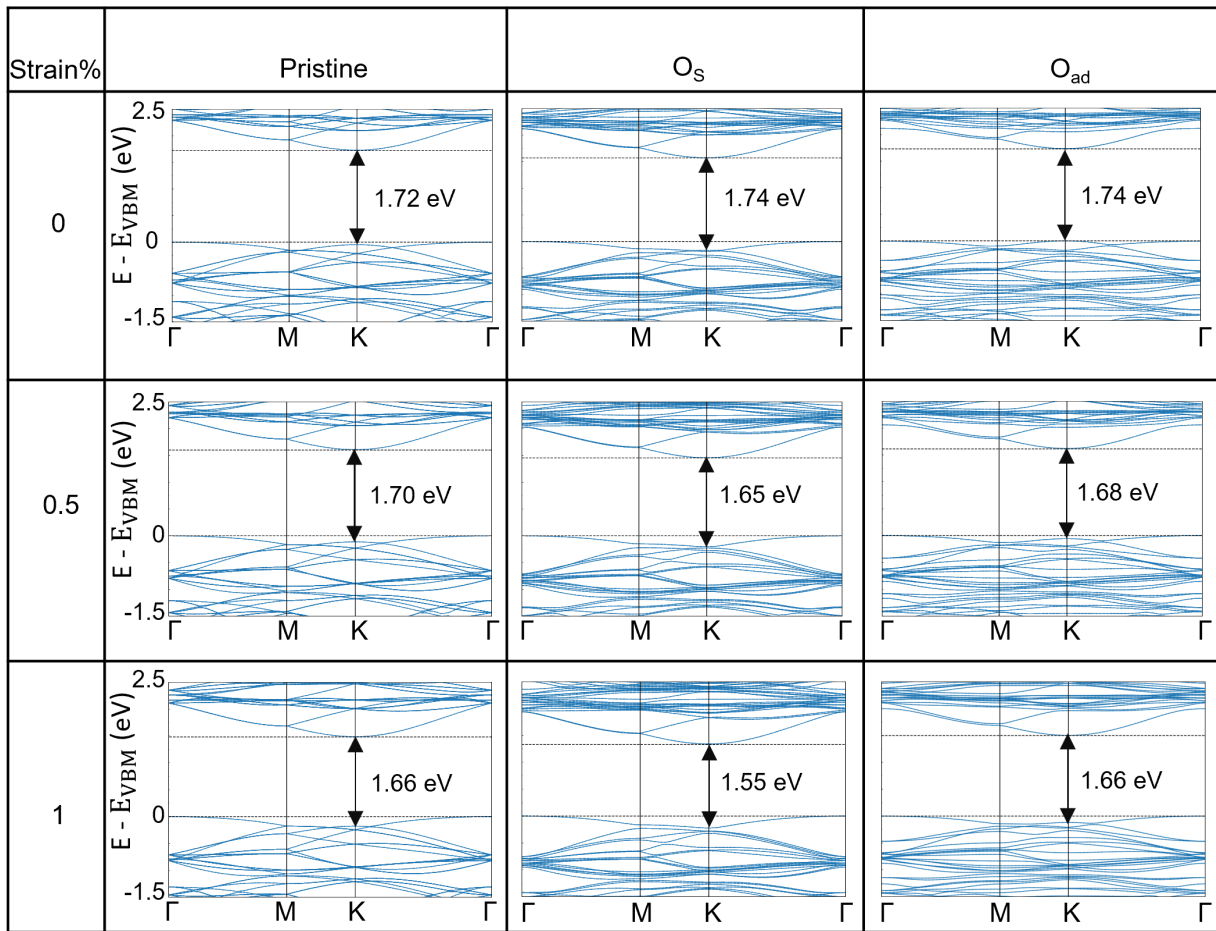


Figure S-VII. Band structures for Pristine ML-MoS₂, with O_S and O_{ad} at different applied strains. Dotted black lines indicate band edges. Black arrows indicate K-K bandgap.

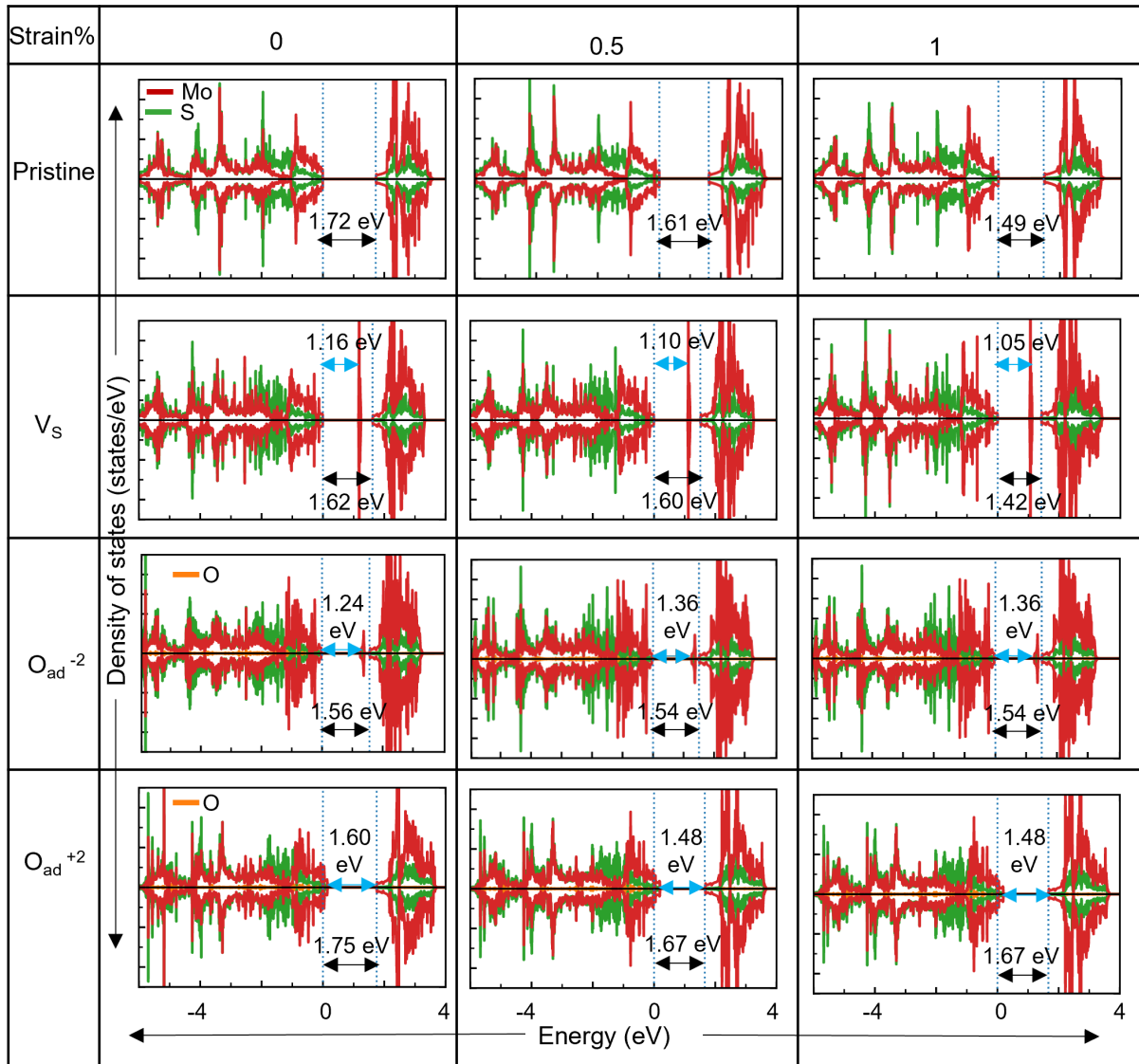


Figure S-VIII. DOS for Pristine ML-MoS₂, and MoS₂ with V_S, O_{ad}⁻² and O_{ad}⁺² at different degrees of applied strain.

Dotted lines indicate band edges. Bandgap magnitudes (black arrows) are indicated along with defect levels (blue arrows) for V_S, O_{ad}⁻² and O_{ad}⁺².

VII) Power dependent photoluminescence spectroscopy of hBN covered and encapsulated samples:

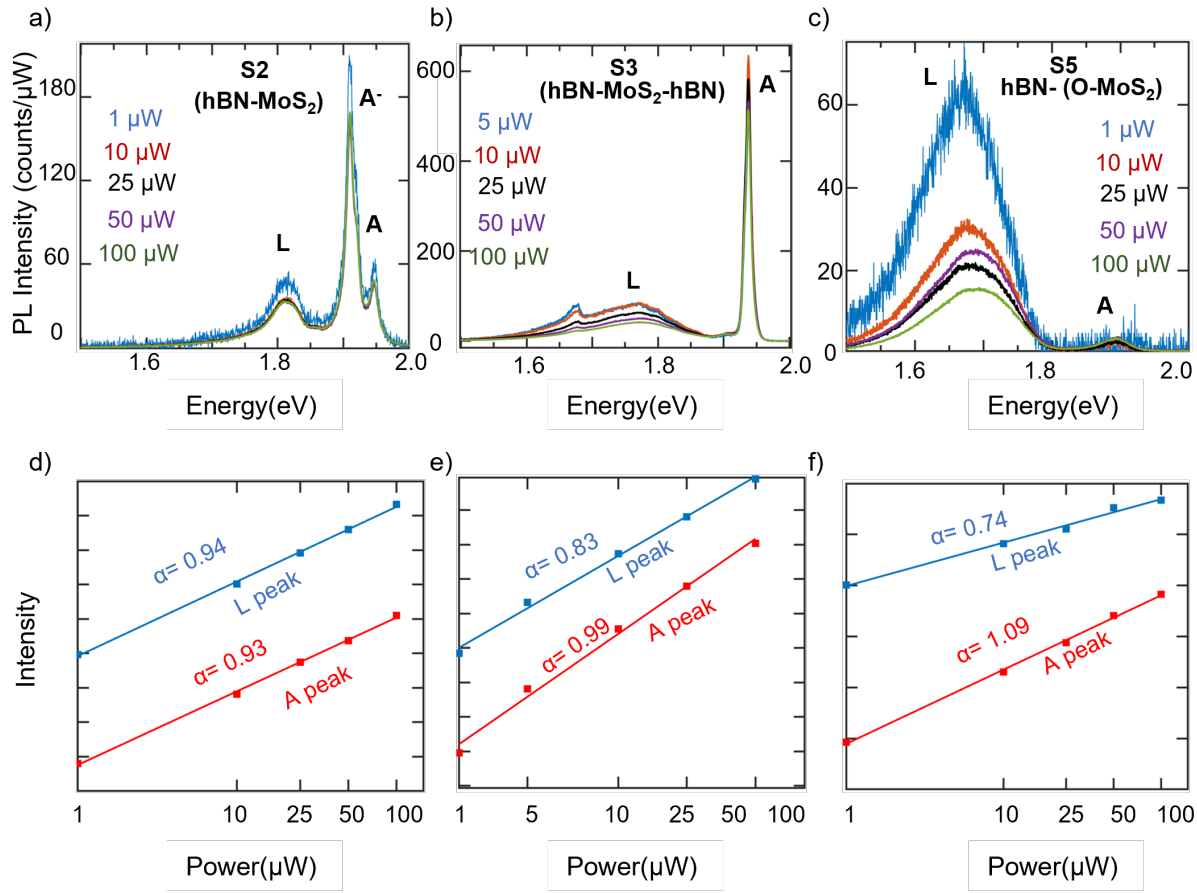


Figure S-IX. Power dependent photoluminescence (PL) spectra of a) S2 b) S3 c) S5 and log intensity v/s log power plots for d) S2 e) S3 and f) S5. All measurements were taken at 4K.

Figure S-IX shows normalized power dependent spectra of samples from S2, S3 and S5. All data is normalized to respective laser power values. The L peak behaves similarly in S3 and S5, but differently in S2 which has a nearly linear behavior. This can also be seen from the slope values in Figure S-IX d-f and inset of Figure 5a and 5b. The similarity in the peak behavior indicates similar origin of luminescence across the samples, but modified defect densities.

In S1, the power-normalized PL for L-peak for 25 μW is lower than power-normalized PL for 50 and 100 μW (see Figure 5a in main text). We note that in case of saturation of defects, the power-normalized PL should reduce with increasing power. On the other hand, if there is no saturation, power-normalized PL

should remain constant with increasing power. Thus power-normalized PL for 25 μ W is anomalous compared to 50 and 100 μ W (by \sim 10 %), and is most probably linked to small sample inhomogeneity. The overall trend is still valid, and shows the low saturation of L-peak in S1 (c.f. S4).

VIII) Temperature dependent PL spectra of hBN covered and encapsulated samples:

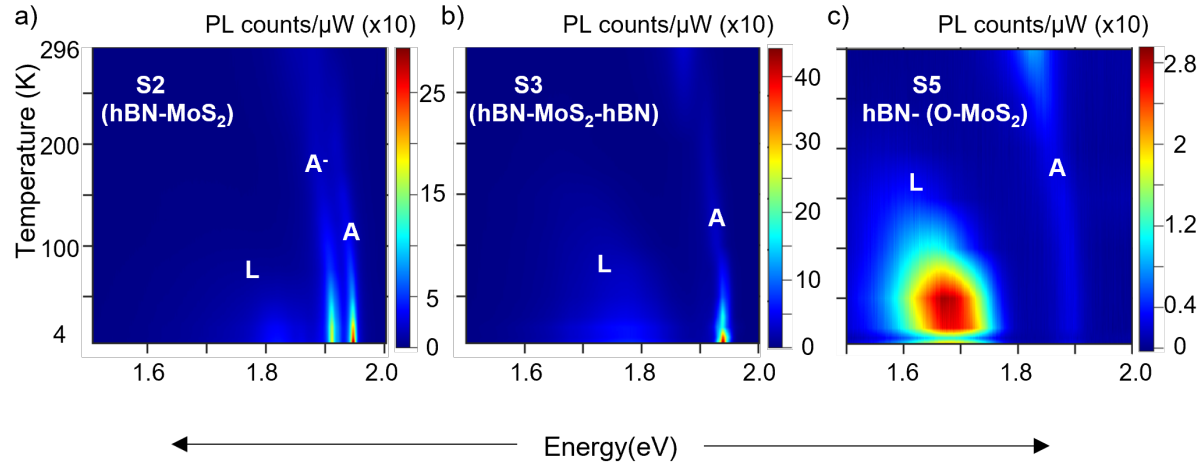


Figure S-X. Surface plots showing evolution of PL spectra with temperature for a) S2 b) S3 c) S5. Measurements were taken at 100 μW for S2 and S3 (same as S1 in Main text Figure 5), whereas 25 μW was used for S5 (same as S4 in Main text Figure 5).

Temperature dependent PL spectra of samples S2, S3 and S5 are shown in Figure S-X. For samples from S1-S3, both the A-excitonic peak and L-peak increases intensity as the temperature decreases with L-peak starting to appear at T~150 K. In S2 and S3, the L-peak intensity is comparatively less, as was observed in previous figures. S5 retains the behavior of S4 with A-exciton PL intensity decreasing with temperature, while L-peak intensity increases.

IX) Comparison of room temperature Raman spectra:

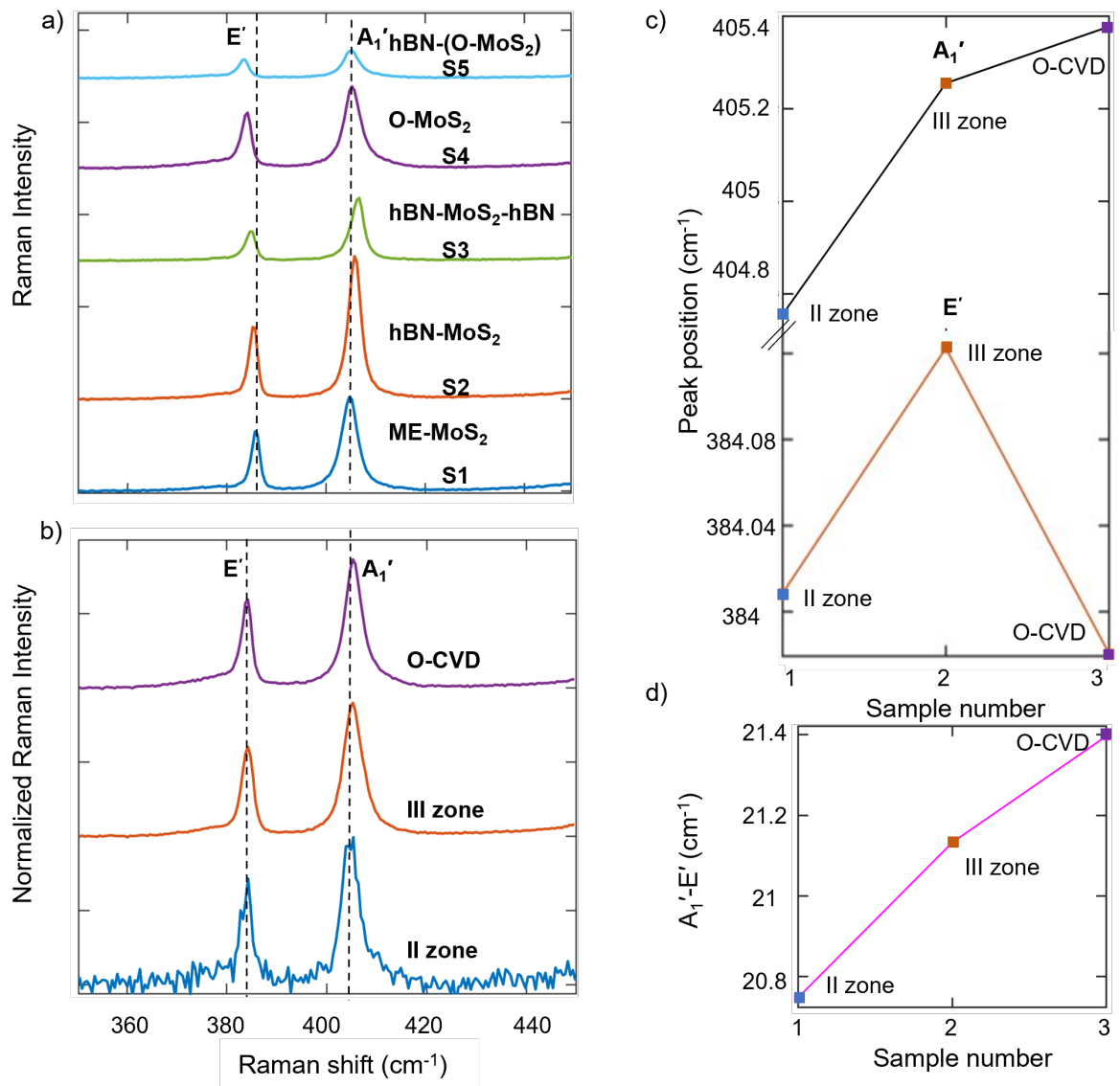


Figure S-XI. a) Background-subtracted Raman spectra of samples S1-S5. All data were taken at same acquisition conditions. The changes in the intensity of the peaks could be due to the presence of hBN. b) Comparison of Raman spectra c) Peak positions of A_{1'} and E' vibrational modes in Raman spectra and d) Difference between A_{1'} and E' peaks in Raman spectra in samples synthesized at different conditions using CVD. Raman intensity values are background subtracted and normalized to respective A_{1'} peak intensity.

Figure S-XI (a) shows the background-subtracted Raman spectra of samples S1-S5, to show changed intensity for different samples. Background was calculated by averaging data in the spectral range away ($340\text{-}360\text{ cm}^{-1}$ range) from main Raman peaks, and then subtracted from raw Raman spectra. Figure S-XI (b-d) compares the results of Raman spectroscopy on samples synthesized at different experimental conditions using CVD. In II zone CVD, the substrate is kept horizontally above the MoO_3 precursor boat while in III zone and O-CVD the substrate is kept vertically in a separate zone at a different temperature than the MoO_3 zone. No oxygen was used in samples other than O-CVD. The E' peak doesn't seem to have evident shift confirming that the peak shift observed in Figure 6 is due to thermal strain. At the same time, A_1' peak increases slightly indicating the possibility of increased doping in O-CVD sample due to the presence of oxygen.

XI) XPS spectra of ML- MoS₂ synthesized using O-CVD and mechanical exfoliation:

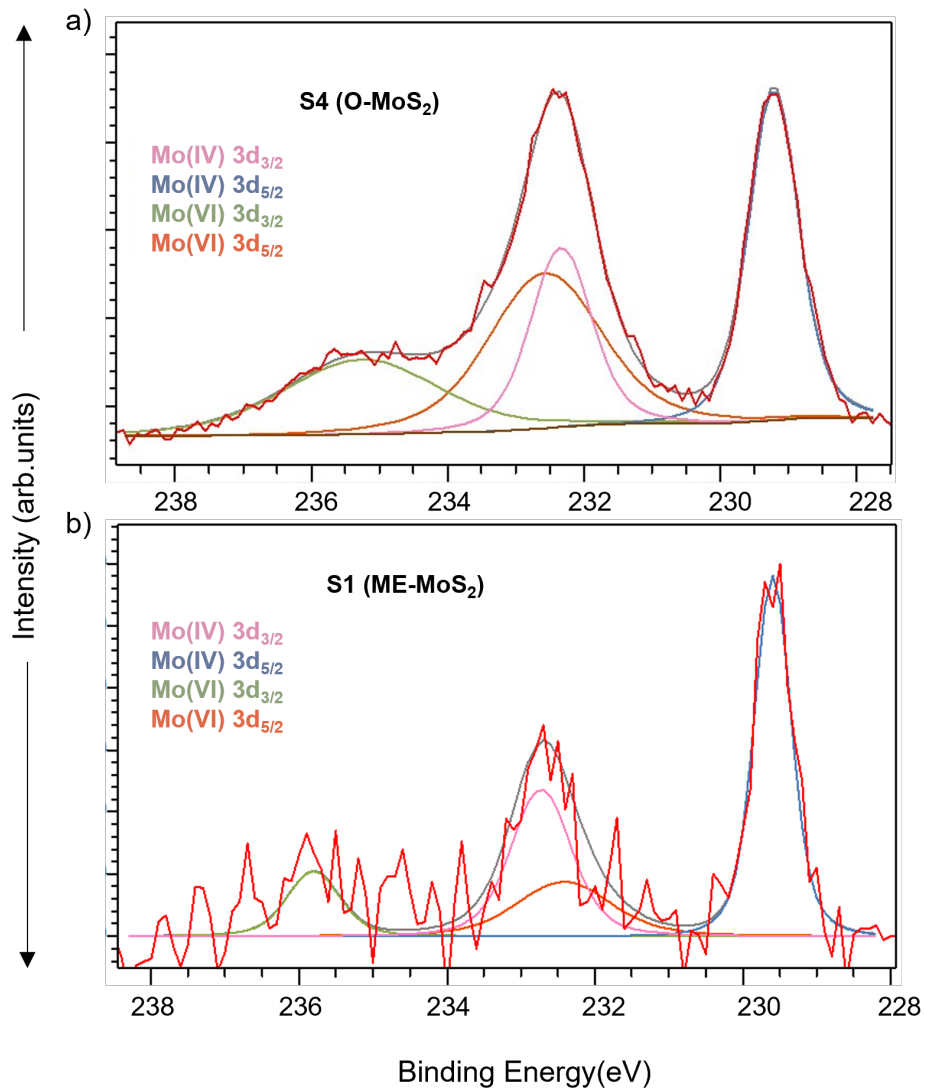


Figure S-XII. X-ray photoelectron spectroscopy (XPS) spectra of O-CVD and mechanically exfoliated ML-MoS₂ samples. a) Mo3d scan of ML MoS₂ synthesized using O-CVD b) Mo3d scan of ML MoS₂ obtained using mechanical exfoliation.

Name	Position		FWHM		Weight percentage	
	S4	S1	S4	S1	S4	S1
Mo IV 3d 3/2	232.34	232.73	1.07	0.96	19.48	28.91
Mo IV 3d 5/2	229.21	229.60	0.87	0.59	29.22	43.37
Mo VI 3d 3/2	235.26	235.80	2.71	0.84	20.52	11.09
Mo VI 3d 5/2	232.57	232.42	1.95	1.50	30.78	16.63

Table S-II. Fitted values from XPS spectra of S1 and S4.

To understand the chemical environment of the samples, including the presence of chemisorbed oxygen in the O-CVD sample and finding its concentration, finding the stoichiometry, and comparing the composition of different samples, XPS was performed (Figure S-XII). We observed that apart from MoS₂ peaks: Mo⁴⁺ 3d_{3/2}, Mo⁴⁺ 3d_{5/2}, there were two other peaks corresponding to Mo⁶⁺3d_{3/2} and Mo⁶⁺ 3d_{5/2} indicating the presence of Mo-O bonds in both samples. The peak positions, FWHM and weight percentages are listed in Table S-II. Interestingly, the Mo⁶⁺ peak is red shifted by 0.54 eV (3d_{3/2}) while Mo⁴⁺ peaks are red shifted by 0.39 eV in the CVD sample. This might be indicative of lower n-type doping in the O-CVD sample.⁹ The atomic percentage of Mo⁴⁺ peaks combined is 48.7 and 72.28 for O-MoS₂ and exfoliated samples respectively and the percentage of Mo⁶⁺ peaks are 51.3 and 27.72 respectively. The values obtained for Mo⁶⁺ 3d_{5/2} for exfoliated samples is not considered for comparison because of the noisy nature of the data. The increased percentage of Mo⁶⁺ peaks indicate increase in Mo-O bonds in the O-CVD sample. The Mo-O bonds in the exfoliated sample could be from physisorbed oxygen. Even though the exfoliated sample data is not of very high quality because of difficulty in performing XPS on an isolated 30 μm flake, the obtained values suggest different origins of oxygen (peak shift, difference in FWHM, changes in atomic percentage) confirming the presence of chemisorbed oxygen in the O-CVD sample.^{9,10}

XI) Room temperature PL spectra from multiple flakes on the O-CVD sample:

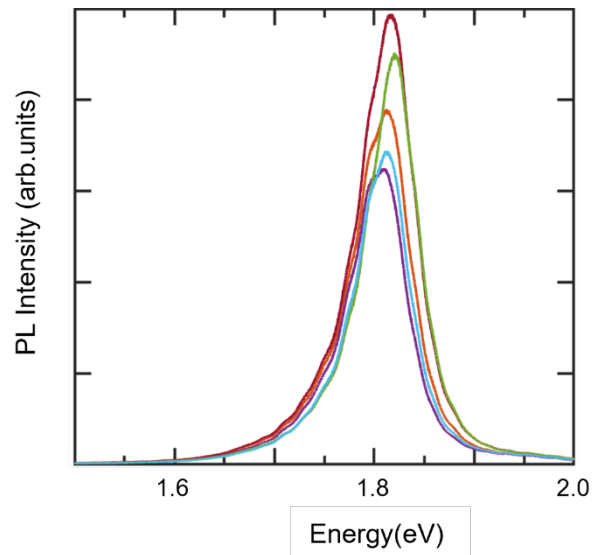


Figure S-XIII. Room temperature PL spectra collected from different flakes on O-CVD sample showing consistency of the obtained PL counts across the synthesized sample.

XII) PL spectroscopy of O-CVD MoS₂ after hBN covering and annealing in glovebox:

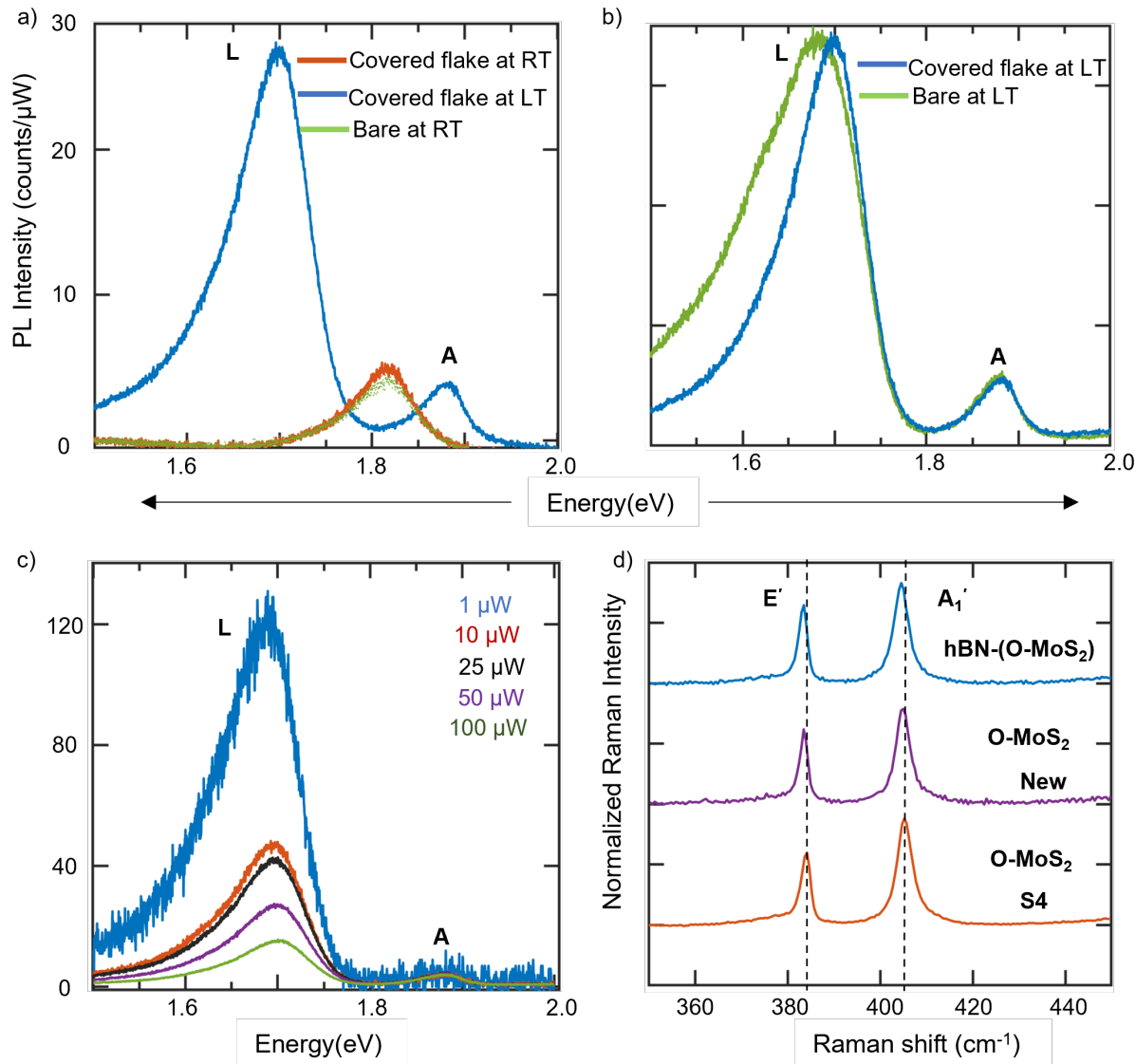


Figure S-XIV. a) Comparison of PL spectra at RT and LT before and after hBN covering b) Comparison of LT PL spectra of bare and covered flake (after the covering process). c) Power dependent PL spectra and c) Comparison of RT Raman spectra of hBN covered O-CVD sample annealed in glovebox.

Figure S-XIV a show the PL spectra of O-CVD sample after hBN covering and annealing was done in glovebox. We observed that similar to S5, the exciton intensity did not decrease after covering in this sample as well. This confirms the stability of the properties in the O-CVD sample despite the annealing conditions. We also observe an additional \sim 16 meV shift of the A exciton peak to the lower energy in comparison to

S4 and S5, and a decrease in the FWHM of the L-peak in covered flake in comparison to the bare flake in the same sample (Figure S-XIV b). The decrease in FWHM indicates improvement in the quality of the sample after hBN covering. This could be because of the elimination of hydrocarbon complexes in the covered material as discussed before. The power dependent spectra (Figure S-XIV c) show saturation of L peak with power suggesting similar defect population in the sample as S4 and S5. Figure S-XIV d shows comparison of Raman spectra of bare and covered flake with S4. There is a slight shift of E' peak and A₁'peak. The peak difference of the new sample is nearly the same as S4.

XIII) Origin of L peak in exfoliated and O-CVD MoS₂ samples:

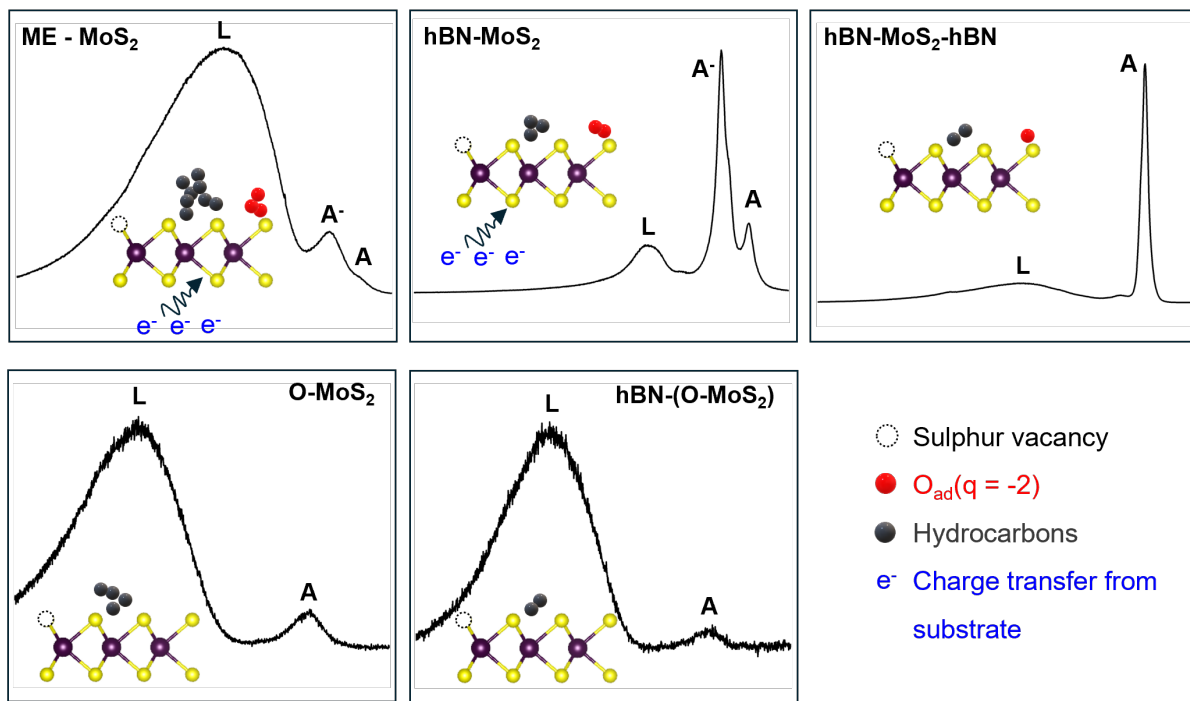


Figure S-XV: Schematics showing the factors contributing to different peaks in the LT PL spectra of samples S1-S5. The variations in the peak intensities can be directly related to the variations in type and amount of defects present in the samples. The defects contributing to L peak in exfoliated sample are sulphur vacancies, charged oxygen adatoms and hydrocarbon complexes and in O-CVD sample are sulphur vacancies and hydrocarbon complexes since charged oxygen adatom formation is less likely at the growth temperature. The importance of hBN covering and encapsulation

in reducing adatoms and hydrocarbon complexes are clearly visualized. These observations are supported by results from formation energy, DOS and band structure calculations.

XIV) Fitted parameters of L-peak and A-peak from LT PL spectra of samples from S1-S5:

Sample	Peak position for A-exciton (A-trion), meV	Peak position (L-peak)	FWHM (A-exciton) (meV)	Integrated intensity (A-exciton) (counts)	Integrated intensity (L-peak) (counts)
S1	1948 (1916)	1797	50	1.02e5	8.97e6
S2	1945 (1912)	1818	20	1.93e5	8.22e5
S3	1939 (1904)	1766	15.6	1.54e6	3.64e6
S4	1891	1672	60	6.18e4	1.28e6
S5	1890	1679	62	5.75e4	7.43e5

Table S-III. Extracted values of L-peak and A-peak from LT PL spectra of samples S1-S5.

Table S-III shows the extracted values of peak position, FWHM and integrated intensities of L-peak and A-peak in the LT PL spectra of samples S1-S5. All the data used for fitting were taken at 100 μW laser power. The L-peak in S1, S4 and S5 were fitted using three peaks and the integrated intensity is the sum of all the peaks. The reported peak position of L-peak in S1, S4 and S5 are the maximum intensity point of the broad peak. In S2 and S3, since L peak intensity was much less than trion and exciton peaks, only one peak was used for fitting. Trion peak was indistinguishable from exciton peak in S3, S4 and S5, and thus were fitted using a single peak while it was fitted using separate peaks in S1 and S2.

XVI) Fitted parameters of A and B exciton peak from RT PL spectra of samples from S1-S5:

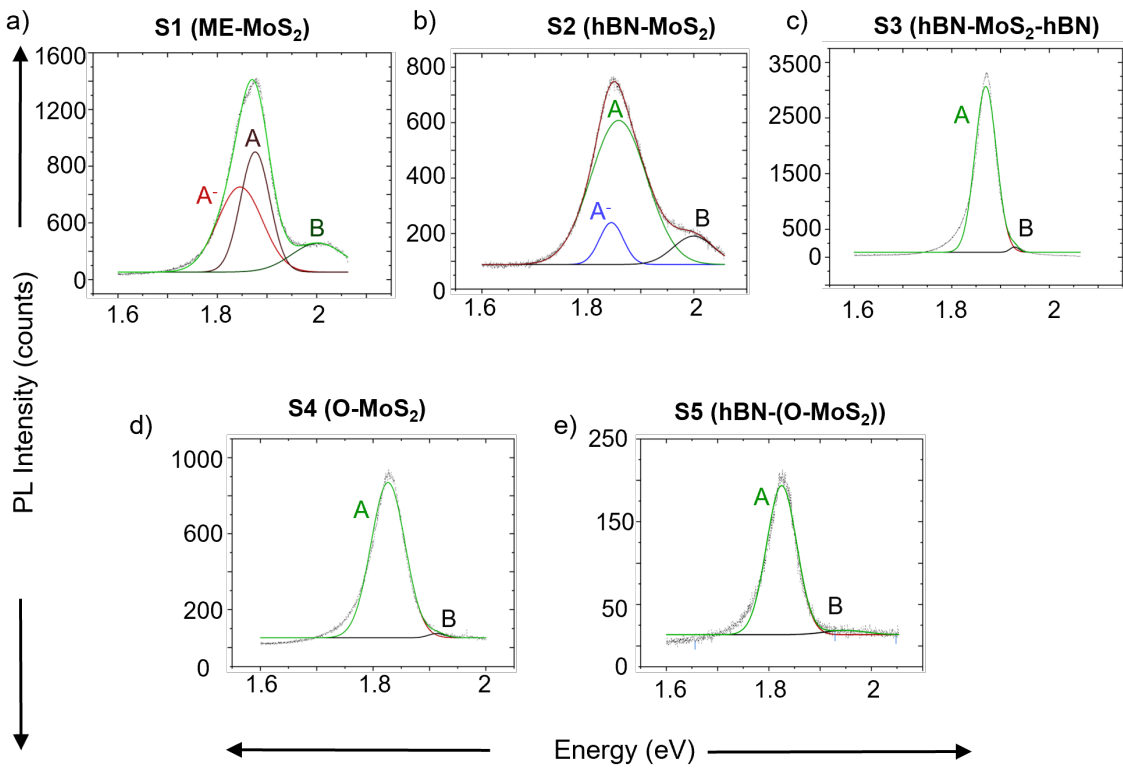


Figure S-XVI. Fitted room temperature (RT) PL spectra of samples a) S1 b) S2 c) S3 d) S4 e) S5.

Sample	Peak position for A-exciton (A-trion), meV	Peak position (B-exciton)	Integrated intensity for A- exciton, counts (percentage)	Integrated intensity for B- exciton, counts (percentage)
S1	1858 (1844)	1999	9.32e3 (66.7%)	6.62e2 (~5%)
S2	1876 (1846)	2002	1.79e4 (71%)	1.78e3 (7.1%)
S3	1872	1929	3.38e4 (96%)	1.35e3 (4%)
S4	1826	1913	1.74e4 (~98%)	2.63e2 (~2%)
S5	1825	1949	5.07e3 (94.5%)	2.93e2 (~5.5%)

Table S-IV. Extracted values of A and B excitonic peak from RT PL spectra of samples S1-S5.

Figure S-XVI shows the fitted RT PL spectra of samples S1-S5. The extracted values of A and B exciton peaks are given in Table S-IV. However, samples S3-S5 doesn't have a pronounced B exciton peak. Thus, the fitting for B-exciton peak in these samples would not be accurate.

References:

1. Sai Gautam, G., Senftle, T. P. & Carter, E. A. Understanding the Effects of Cd and Ag Doping in Cu₂ZnSnS₄ Solar Cells. *Chem. Mater.* **30**, 4543–4555 (2018).
2. Malitckaya, M., Komsa, H.-P., Havu, V. & Puska, M. J. First-Principles Modeling of Point Defects and Complexes in Thin-Film Solar-Cell Absorber CuInSe₂. *Advanced Electronic Materials* **3**, 1600353 (2017).
3. Sun, J., Ruzsinszky, A. & Perdew, J. P. Strongly Constrained and Appropriately Normed Semilocal Density Functional. *Phys. Rev. Lett.* **115**, 036402 (2015).
4. Car, R. Fixing Jacob's ladder. *Nature Chem* **8**, 820–821 (2016).
5. Kumagai, Y. & Oba, F. Electrostatics-based finite-size corrections for first-principles point defect calculations. *Phys. Rev. B* **89**, 195205 (2014).
6. Broberg, D. *et al.* PyCDT: A Python toolkit for modeling point defects in semiconductors and insulators. *Computer Physics Communications* **226**, 165–179 (2018).
7. Informatics, N. O. of D. and. NIST Chemistry WebBook. <https://webbook.nist.gov/chemistry/>.
8. Zhou, W. *et al.* Intrinsic Structural Defects in Monolayer Molybdenum Disulfide. *Nano Lett.* **13**, 2615–2622 (2013).
9. Shen, P.-C. *et al.* Healing of donor defect states in monolayer molybdenum disulfide using oxygen-incorporated chemical vapour deposition. *Nat Electron* **5**, 28–36 (2022).
10. Durairaj, S. *et al.* Oxygen-Driven Growth Regulation and Defect Passivation in Chemical Vapor Deposited MoS₂ Monolayers. *Crystal Growth & Design* **21**, 6793–6801 (2021).